Nanoscale Advances

ROYAL SOCIETY OF CHEMISTRY

PAPER

View Article Online
View Journal | View Issue

Cite this: *Nanoscale Adv.*, 2025, **7**, 3068

Enzyme-triggered aggregation of upconversion nanoparticles for targeted photodynamic therapy *via* NIR irradiation†

Bo Ling,‡[ab] Yaguang Wang,‡[c] Huaze Dong,[a] Hongqi Chen *[b] and Lun Wang *[b]

A core–shell–shell nanoplatform responsive to alkaline phosphatase (ALP) was developed for efficient tumor targeting and near-infrared (NIR)-activated photodynamic therapy (PDT). Specifically, UCNP@SiO_2-Bodipy@FFYp was synthesized by encapsulating upconversion nanoparticles (UCNPs) within a silica shell, embedding bodipy derivatives as photosensitizers, and covalently attaching a phosphorylated peptide (FFYp). Förster resonance energy transfer (FRET) from the UCNP emission at 550 nm to bodipy facilitated reactive oxygen species (ROS) generation upon NIR excitation. In the tumor microenvironment, ALP-triggered dephosphorylation converted UCNP@SiO_2-Bodipy@FFYp into the more hydrophobic UCNP@SiO_2-Bodipy@FFY, thereby promoting tumor cell uptake and tumor-specific accumulation. By leveraging this ALP-responsive targeting strategy alongside the deep-tissue penetration of NIR light, significant tumor growth inhibition was achieved both *in vitro* and *in vivo*. Notably, after 15 days of treatment in Balb/c mice bearing HeLa tumors, the tumor volume was reduced by over 95%. Taken together, these results highlight the promise of UCNP@SiO_2-Bodipy@FFYp as a tumor-responsive nanoplatform for highly effective, targeted PDT in cancer therapy.

Received 20th December 2024
Accepted 20th March 2025

DOI: 10.1039/d4na01050g

rsc.li/nanoscale-advances

1. Introduction

Photodynamic therapy (PDT) has garnered significant attention in clinical tumor treatments due to its ability to precisely control the treatment site and effectively destroy tumors with minimal invasiveness. This targeted approach offers considerable advantages compared to traditional chemotherapy and radiotherapy, leading to improved patient outcomes with reduced side effects.[1–4] Photosensitizers lacking tumor-targeting capabilities will disperse throughout the body, resulting in insufficient drug accumulation in the tumor, while increasing drug concentration may lead to excessive renal burden.[5–7] To enhance the spatial accuracy of PDT, photosensitizers with tumor-targeting ability and strong near-infrared (NIR) absorption are highly sought after.[8–12] Additionally, enhancing the tumor-targeting of photosensitizers can further protect normal cells at tumor margins.[13,14] Conversely, NIR light provides deep tissue penetration and high biosafety because biological tissues absorb it only weakly.[15] However, conventional photosensitizers, such as chlorin e6,[16] zinc phthalocyanine,[17] 5-aminolevulinic acid,[18] and rose bengal,[19] not only exhibit insufficient tumor-targeting, but also have excitation wavelengths limited to visible light or even ultraviolet light, which severely restricts their therapeutic effectiveness for extensive or deep-seated tumors. Nevertheless, few organic NIR (λ_{ex} > 800 nm) photosensitizers have been reported, because the too low energy gap causes them to be more inclined to release energy in a non-radiative process, resulting in extremely low reactive oxygen species (ROS) yields. Therefore, the development of NIR photosensitizers with precise tumor-targeting and good biocompatibility is of great significance but still requires extensive exploration. However, the above limitations can be circumvented by adhering the photosensitizer to the surface or shell of upconversion nanoparticles (UCNPs) with tumor-targeting ability.

Lanthanide-doped UCNPs are in high demand owing to their numerous advantages, including a significant anti-Stokes shift, tunable emission spectra, extended decay lifetimes, and minimal cytotoxicity.[20–23] When organic photosensitizers are adhered to the surface or shell of UCNPs, these UCNPs can serve as absorbing antennae and converters for NIR light. They absorb and convert NIR light into visible light and subsequently transfer this converted light to short-wavelength organic photosensitizers through the fluorescence resonance energy transfer (FRET) effect. This compensates for the limitations of

[a]*Department of Chemistry and Pharmaceutical Engineering, Hefei Normal University, Hefei, 230061, China*

[b]*Anhui Province Key Laboratory of Biomedical Materials and Chemical Measurement, Key Laboratory of Functional Molecular Solids, Ministry of Education, College of Chemistry and Materials Science, Anhui Normal University, Wuhu, 241002, China. E-mail: hq80chen@mail.ahnu.edu.cn; wanglun@mail.ahnu.edu.cn*

[c]*Department of Anesthesia and Perioperative Medicine, The Second Affiliated Hospital Anhui Medical University, Hefei, 230000, China*

† Electronic supplementary information (ESI) available. See DOI: https://doi.org/10.1039/d4na01050g

‡ These authors contributed equally to this work.

current organic photosensitizers, which are restricted to visible light excitation.[24–27]

In this study, we observed that alkaline phosphatase (ALP) is over-expressed on the membrane structures of certain cancer cell lines, including TCam-2, HepG2, HeLa, and MCF-7, making it a reliable biomarker for cancer diagnosis.[28–30] Thus, UCNPs modified with the short synthesized peptide FFYp (Phe-Phe-Tyr-$(PO(OH)_2)$-OH) could be harnessed for targeted accumulation in malignant tumor cells following the dephosphorylation of the substrate and the subsequent self-assembly.[31] Herein, an ALP-triggered UCNP@SiO_2-Bodipy@FFYp system, which absorbs NIR at 980 nm and targets and accumulates in tumours upon ALP dephosphorylation, was rationally designed through the adsorption of UCNPs and a classical organic photosensitizer, Bodipy-I, on porous SiO_2. Our UCNP@SiO_2-Bodipy@FFYp not only functions as a PDT reagent but also enhances the hydrophobicity of UCNPs to promote better aggregation. Upon introduction into the tumor microenvironment, UCNPs@SiO_2-Bodipy@FFYp undergoes dephosphorylation by the secreted ALP, resulting in the more hydrophobic product UCNP@SiO_2-Bodipy@FFY (Phe-Phe-Tyr-OH) (Fig. 1), which is then internalized by tumor cells and accumulates within them. Upon 980 nm irradiation, FRET from the upconversion fluorescence emission of the UCNPs at 550 nm is directed toward the photosensitizer Bodipy-I which has a high ROS generation capability, leading to significant tumor regression and minimal side effects. These findings demonstrate that engineered peptide-modified multifunctional nanoplatforms are capable of targeting aggregation in tumor cells expressing higher levels of ALP enabling NIR-induced *in vivo* PDT for cancer treatment.

2. Experimental

2.1 Materials

Sigma-Aldrich supplied $(CH_3CO_2)_3Y\cdot xH_2O$, $Yb(C_2H_3O_2)_3\cdot 4H_2O$, and $(CH_3CO_2)_3Er\cdot xH_2O$ each with 99.9% purity. Oleic acid (OA), sodium hydroxide (NaOH), 1-octadecene (ODE), 1,3-diphenylisobenzofuran (DPBF), *N*,*N*-(3-(dimethylamino)propyl)-*N*-ethylcarbodiimide (EDC), *N*-hydroxysuccinimide (NHS), phenylacetylene, triethylamine, $Pd(PPh_3)_2Cl_2$, CuI, and 2,6-diiodo-1,3,5,7-tetramethyl-8-phenyl-4,4-difluoroboradiazaindacene were obtained from Aladdin Reagent (Shanghai, China). Tetrahydrofuran (THF), dichloromethane (DCM), NH_4F (AR), ethanol (AR), cyclohexane (AR) and *N*,*N*-dimethylformamide (DMF) were purchased from Sinopharm Chemical Reagent Co. Ltd (Shanghai, China) Sinopharm. A Cell Counting Kit-8 (CCK-8), 2,7-dichlorodihydrofluorescein diacetate (DCFH-DA), calcein acetoxymethyl ester (Calcein AM), and propidium iodide (PI) were obtained from Beyotime.

2.2 Sample characterization techniques

Transmission electron micrographs (TEM) were acquired using a JEOL 2100 high-resolution transmission electron microscope operating at 200 kV. The photophysical properties of the nanoparticles (NPs) were evaluated using a Shimadzu UV-3600 spectrophotometer and a Hitachi FL-4600 fluorescence spectrophotometer (equipped with a 980 nm laser). The concentrations of Yb, Y, Si, P, and I elements were quantified using Inductively Coupled Plasma Optical Emission Spectroscopy

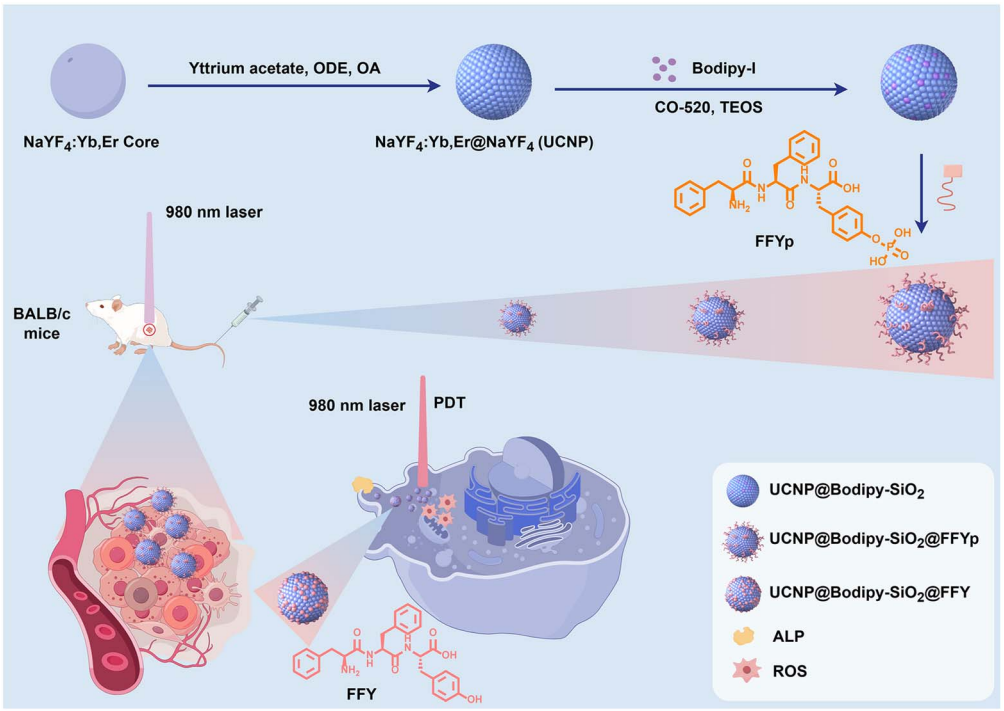

Fig. 1 Schematic illustration of ALP-triggered UCNP@SiO_2-Bodipy@FFYp for tumor-targeted photodynamic therapy (PDT). Portions of the graphical materials were provided by Figdraw.

(ICP-OES, Avio 220 Max, PerkinElmer) following microwave-assisted digestion (WX-8000, PreeKem, Shanghai, China). ^{1}H NMR spectra were obtained on a Bruker AV 400. Zeta potential was measured and dynamic light scattering (DLS) was conducted using a NanoBrook 90Plus PALS. Cell viability was assessed with a spectrophotometer (Biotek Synergy H1, USA). Fluorescence images of the cells were captured using an IX83 Olympus microscope.

2.3 Synthesis of $NaYF_4$:Yb,Er@$NaYF_4$ core–shell nanoparticles

$NaYF_4$:49%Yb,1%Er@$NaYF_4$ wrapped in oleic acid was synthesized as reported in our previous work.[32] Briefly, yttrium acetate (0.200 mmol), ytterbium acetate (0.196 mmol), and erbium acetate (0.004 mmol) were mixed with 1-octadecene (ODE, 6.00 mL) and oleic acid (OA, 4.00 mL) in a two-neck flask. Subsequently, the $NaYF_4$ shell was formed using a process similar to that used to synthesize the $NaYF_4$:49%Yb,1%Er core, using yttrium acetate (0.200 mmol), ODE (7.00 mL), and OA (3.00 mL). Finally, $NaYF_4$:49%Yb,1%Er@$NaYF_4$ wrapped in oleic acid was obtained and subsequently dispersed in cyclohexane for further experiments.

2.4 Synthetic route of Bodipy-I

The compound 2,6-diiodo-1,3,5,7-tetramethyl-8-phenyl-4,4-difluoroboradiazaindacene was synthesized according to procedures outlined in the literature. Bodipy-I was then synthesized *via* a method described in the literature.[33] In detail, 114.0 mg (0.100 mmol) of 2,6-diiodo-1,3,5,7-tetramethyl-8-phenyl-4,4-difluoroboradiazaindacene and 22.0 mg (0.100 mmol) of phenylacetylene were dissolved in a mixture of THF/triethylamine (40.00 mL, v/v = 1 : 1). Then, 7.0 mg (0.005 mmol) of $Pd(PPh_3)_2Cl_2$ and 4.0 mg (0.010 mmol) of CuI were added after removing oxygen by purging with argon. After a 4 h reflux, the mixture was purified by column chromatography (silica gel, CH_2Cl_2/hexanes, 1/2, v/v), yielding a deep-red solid.

2.5 Synthesis of Phe-Phe-Tyr-($PO(OH)_2$)-OH (FFYp)

Phe-Phe-Tyr-($PO(OH)_2$)-OH (FFYp) was synthesized *via* solid-phase peptide synthesis (SPPS)[31] following the synthetic pathway illustrated in Fig. S1 in the ESI.†

2.6 Synthesis of UCNP@Bodipy-SiO_2

By employing a modified reverse microemulsion methodology,[8] we synthesized the UCNP@SiO_2-Bodipy composite, as depicted in Fig. S2a in the ESI.† In a 50.0 mL flask, we mixed 0.80 mL of Igepal CO-520 with 20.00 mL of cyclohexane and stirred the mixture for 1 h at 22 °C. Subsequently, 10.0 mg of $NaYF_4$:49% Yb,1%Er@$NaYF_4$ dissolved in cyclohexane was added, and the mixture was stirred for an additional 2 h. Then, 50 μL of a 1 mg per mL Bodipy aqueous solution was added, and the mixture was agitated for 1 h. A gradual addition of 0.15 mL of $NH_3 \cdot H_2O$ was performed, followed by the gradual addition of 0.20 mL of TEOS, and the mixture was stirred for an additional 24 hours. The resulting UCNP@SiO_2-Bodipy products were subjected to multiple washes with ethanol and subsequently resuspended in 1.00 mL of ethanol.

2.7 Preparation of FFYp modified UCNP@SiO_2-Bodipy

$NaYF_4$:Yb,Er@$NaYF_4$@SiO_2-Bodipy@FFYp was fabricated, as shown in Fig. S2b–d in the ESI.† In the initial step, surface modification with amino groups was performed as follows. UCNP@SiO_2-Bodipy dissolved in ethanol was rapidly mixed with 0.50 mL of APTES with vigorous stirring, followed by overnight incubation, resulting in the formation of amino-functionalized UCNP@SiO_2-Bodipy. Subsequently, these particles were carefully introduced into a flask containing 20.00 mL of 0.100 M succinic anhydride in DMF. The resulting mixture was stirred continuously for 24 h, leading to the formation of carboxyl-functionalized UCNP@SiO_2-Bodipy.

To achieve covalent conjugation of FFYp with UCNP@SiO_2-Bodipy, a slight modification to the EDC/NHS coupling method was employed.[34] Briefly, 0.10 mL of EDC (5.00 mg mL^{-1}) and 100 μL of NHS (5.00 mg mL^{-1}) were added to the carboxyl-modified UCNP@SiO_2-Bodipy (1.00 mg mL^{-1}, 1 mL). The mixture was then slowly stirred at room temperature for 1 h to activate the UCNPs. Subsequently, FFYp was introduced to the activated UCNP solution and incubates at room temperature for 18 h. Finally, the FFYp-modified UCNP@SiO_2-Bodipy was washed three times with PBS (pH 7.4).

2.8 Cellular uptake

HeLa cells were cultured on 35 mm glass-bottomed Petri dishes, in an appropriate culture medium, for 24 hours at 37 °C under 5% CO_2. After three washes with PBS (pH 7.4), HeLa cells were separately incubated in two 1.00 mL aliquots of the culture medium, each containing either 0.050 mg per mL UCNP@SiO_2-Bodipy@FFYp or UCNP@SiO_2-Bodipy nanoprobes, to study their respective uptakes. After five additional washes with PBS to remove any non-internalized material, upconversion luminescence (UCL) images were captured using a 980 nm excitation laser to provide detailed insights into the cellular interactions with the nanoprobe.

2.9 Detection of intra- and extracellular ROS

The production of ROS from UCNP@SiO_2-Bodipy@FFYp upon 980 nm NIR laser excitation was first identified using 1,3-diphenylisobenzofuran (DPBF) as a chemical sensor. This reaction is irreversible and results in a decrease in the characteristic absorbance of DPBF at 420 nm. With increasing NIR illumination time, the DPBF absorbance decreased exponentially, showing a 65% decrease occurring in 30 minutes, indicating the successful generation of extracellular ROS.

Intracellular ROS was measured using the DCFH-DA fluorescence assay. HeLa cells were plated in a 35 mm Petri dish with a culture medium and incubated for 24 hours. Post-treatment with UCNP@SiO_2-Bodipy@FFYp and UCNPs@SiO_2-Bodipy for 4 hours, the cells were treated with DCFH-DA for 20 minutes. After three PBS washes, the cells were exposed to a 980 nm laser (0.8 W cm^{-2}) for 10 minutes with an interval after every minute, after which fluorescence images were captured to

measure $^1O_2$ production. ROS generation is crucial for evaluating the effectiveness of PDT, as cytotoxic ROS can cause DNA and mitochondrial damage, leading to cell apoptosis.

2.10 Cytotoxicity

The cytotoxicity of UCNP@SiO_2-Bodipy@FFYp in HeLa cells was evaluated using the CCK-8 Kit. Solutions of UCNP@SiO_2-Bodipy@FFYp at concentrations of 12.50, 25.00, 50.00, 100.0, and 200.0 μg mL^{-1} in 100 μL of growth medium were added to separate wells of a 96-well plate. The plate was then incubated for 24, 48 and 72 h at 37 °C under 5% CO_2.

Following the incubation period, 10 μL of CCK-8 solution was added to each well of the 96-well plate. After an additional 1 h of incubation with shaking, the absorbance of each well at 450 nm was measured using an ELISA reader (BioTek Synergy H1).

Each experiment was repeated at least three times. Cell viability was calculated using the following formula: viability (%) = (mean absorbance value of the treatment group/mean absorbance value of the control group) × 100.

2.11 Animal experiments

Female Balb/c mice (4–5 weeks old) were obtained from GemPharmatech (Jiangsu, China). All animals were cared for in compliance with the guidelines outlined in the Guide for the Care and Use of Laboratory Animals. All procedures were approved by the Anhui Normal University Animal Care and Use Committee (Permit Number: AHNU-ET2022028). To establish a tumor model, 2×10^6 HeLa cells (100 μL, 10% Matrigel) were subcutaneously injected into the mice.

Balb/c mice bearing HeLa tumors approximately 60 mm^3 in volume were divided into three treatment groups based on the intravenous administration type (n = 5 per group). Group I received PBS treatment, Group II received UCNP@SiO_2-Bodipy (100 mg kg^{-1}) with laser irradiation, and Group III received UCNP@SiO_2-Bodipy@FFYp (100 mg kg^{-1}) with laser irradiation. Groups I and II served as control groups, and Groups II and III were subjected to 980 nm laser irradiation. On days 0 (6 h after injection), 1, 3, and 5, 980-nm laser irradiation was performed. The 980 nm laser was used for a total of 15 minutes (30 seconds irradiation followed by a 1 min break to prevent overheating) with a power density of 0.8 W cm^{-2}. Tumor dimensions and mouse body weight were precisely measured every three days with Vernier calipers and an electronic balance, respectively. Following these measurements, the tumor specimens were harvested and documented through photographic imaging.

The harvested tumor tissues were subjected to a series of analyses, including terminal deoxynucleotidyl transferase-mediated dUTP nick-end labeling (TUNEL), Ki67 antigen detection, and Hematoxylin and Eosin (HE) staining, as observed under a fluorescence microscope. Additionally, paraffin-embedded sections from key organs, including the heart, liver, spleen, lungs, and kidneys, were procured from each group for HE staining. These resulting staining assays

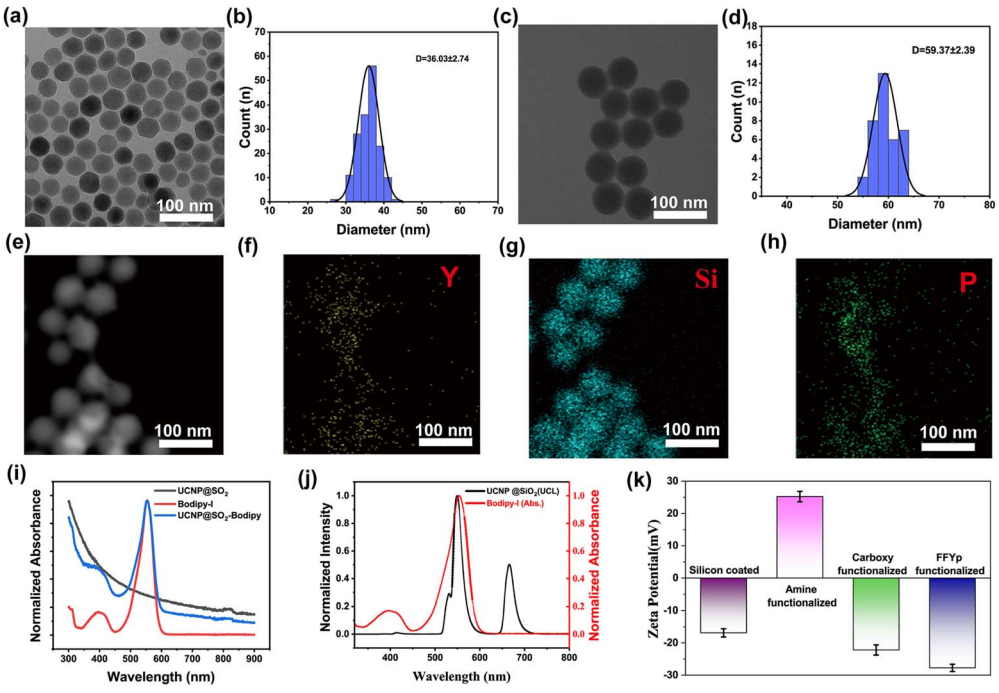

Fig. 2 Characterization and surface charge evaluation of UCNP@SiO_2-Bodipy@FFYp. (a) Transmission electron microscopy (TEM) images of $NaYF_4$:Yb,Er@$NaYF_4$ (UCNP); (b) size distribution of $NaYF_4$:Yb,Er@$NaYF_4$; (c) TEM images of UCNP@SiO_2-Bodipy@FFYp; (d) size distribution of UCNP@SiO_2-Bodipy@FFYp; (e) HAADF-STEM image of UCNP@SiO_2-Bodipy@FFYp and elemental mapping images of (f) Y, (g) Si, and (h) P; (i) UV-vis spectra of UCNP@SiO_2, Bodipy-I, and UCNP@SiO_2-Bodipy; (j) fluorescence spectra of UCNP@SiO_2 and UV-vis spectra of Bodipy-I; (k) zeta potential diagram of different nanoparticles; data are presented as mean ± SD (n = 3).

were then examined using a fluorescence microscope (Olympus).

3. Results

3.1 Characterization of UCNP@SiO_2-Bodipy@FFYp

(1) Bodipy-I, ^{1}H NMR (Fig. S3 in the ESI†) (400 MHz, $CDCl_3$) δ = 7.54–7.52 (m, 3H), 7.46–7.44 (m, 2H), 7.34–7.31 (m, 3H), 7.29–7.27 (m, 2H), 2.71 (s, 3H), 2.66 (s, 3H), 1.50 (s, 3H), 1.40 (s, 3H). ESI-MS calcd for $[C_{27}H_{23}BF_2N_2I]^+$, $[M + H]^+$: 551.1; found $[M + H]^+$: 551.2 (Fig. S4 in the ESI†).

(2) Phe-Phe-Tyr-$(PO(OH)_2)$-OH (FFYp). ^{1}H NMR (Fig. S5 in the ESI†) (400 MHz, d-DMSO) δ = 8.69 (d, J = 8.0 Hz, 1H), 8.52 (d, J = 8.0 Hz, 2H), 7.33–7.18 (m, 10H), 7.13 (d, J = 8.0 Hz, 2H), 7.04 (d, J = 8.0 Hz, 2H), 4.68–4.63 (m, 1H), 4.49–4.43 (m, 1H), 3.81 (brs, 1H), 3.11–3.01 (m, 4H), 2.89–2.73 (m, 4H). MS of compound FFYp: calculated for $C_{27}H_{30}N_3O_8P$, $[M + H]^+$: 556.2; obsvd $[M + H]^+$: 556.0 (Fig. S6 in the ESI†).

(3) UCNP@SiO_2-Bodipy@FFYp. Transmission electron microscopy (TEM) images confirmed the successful synthesis of hexagonal UCNPs with an average particle size of approximately 36.03 nm, as shown in Fig. 2a and b. After coating and modification, the final UCNP@SiO_2-Bodipy@FFYp displayed a uniform spherical shape with an average size of 59.37 nm, as illustrated in Fig. 2c and d. Elemental mapping images (Fig. 2e–h) revealed the presence of Si and P on the nanomaterials' surface, confirming the successful attachment of FFYp to the surface of UCNP@SiO_2-Bodipy. Upon exposure to 980 nm NIR laser irradiation, the UCNPs displayed strong fluorescence at 550 and 665 nm (Fig. 2i). Fig. 2j shows that UCNP@SiO_2 itself has no absorption at 550 nm, but after loading with Bodipy-I, UCNP@SiO_2-Bodipy exhibited an absorption peak at this wavelength. Furthermore, as seen in Fig. S7,† UCNP@SiO_2-Bodipy@FFYp, which has been loaded with Bodipy, shows significant quenching at the 550 nm emission wavelength compared to UCNP@SiO_2-FFYp without Bodipy loading. These results indicate successful Bodipy-I loading. The zeta potential values of UCNP@SiO_2-Bodipy and amine-functionalized UCNP@SiO_2-Bodipy were measured to be −16.9 mV and 25.2 mV, respectively. Subsequent modifications with carboxyl functional groups led to a reduced zeta potential of −22.2 mV in UCNP@SiO_2-Bodipy, and further to −27.5 mV in UCNP@SiO_2-Bodipy@FFYp, as illustrated in Fig. 2k. The measurement conditions for the ICP-OES quantification are shown in Table

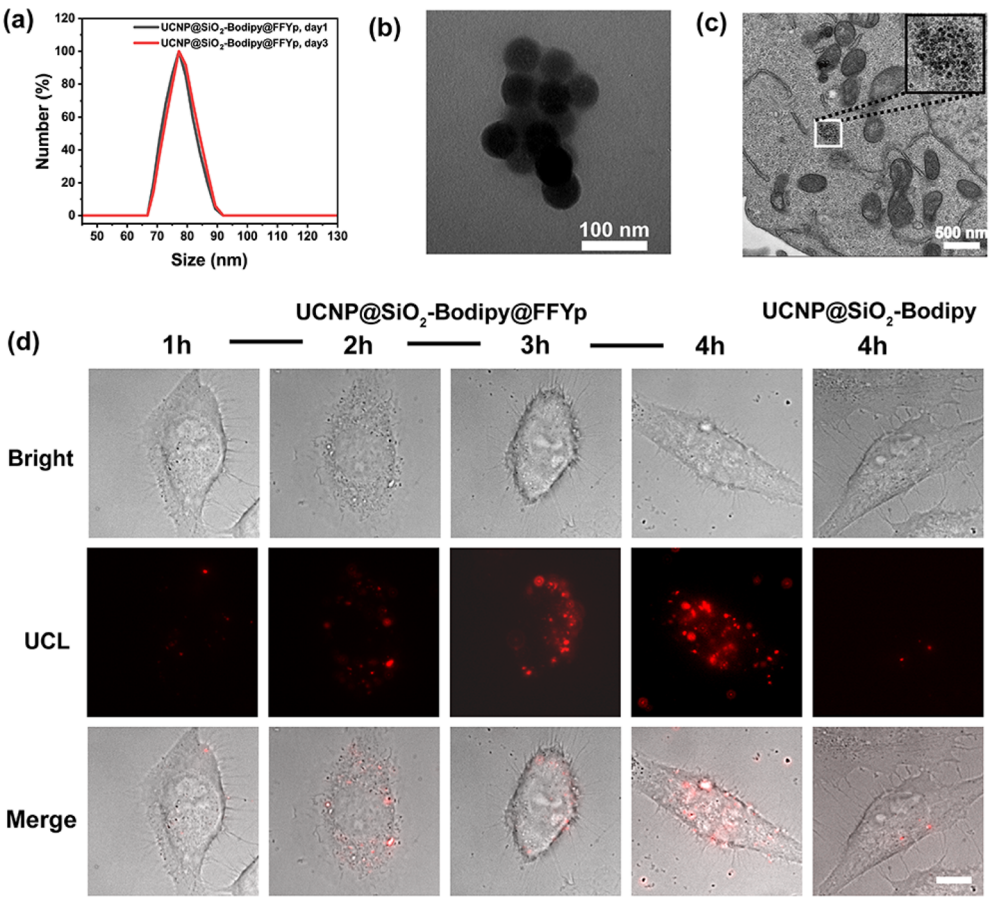

Fig. 3 Cellular uptake of UCNP@SiO_2-Bodipy@FFYp. (a) Hydrodynamic size distribution of UCNP@SiO_2-Bodipy@FFYp in PBS on day 1 and day 3; (b) UCNP@SiO_2-Bodipy@FFYp after incubation with ALP; (c) TEM images of the cell sections; (d) phagocytosis of UCNP@SiO_2-Bodipy@FFYp and UCNP@SiO_2-Bodipy by HeLa cells at indicated time points. The fluorescence from UCNP@SiO_2-Bodipy@FFYp and UCNP@SiO_2-Bodipy was captured using an IX83 Olympus microscope at 100× magnification (Ex: 980 nm, Em: 665 nm). The scale bar represents 10 μm.

S1,† with the results presented in Tables S2 and S3.† The ICP-OES data indicate that Bodipy-I is efficiently encapsulated within the SiO_2 matrix, and enough FFYp peptide is attached to the surface. All results confirm that UCNP@SiO_2-Bodipy@FFYp was successfully synthesized, uniformly coated, and appropriately sized.

3.2 ALP-triggered upconversion nanoparticle aggregation

Stability assessments of UCNP@SiO_2-Bodipy@FFYp dispersions in phosphate-buffered saline (PBS) demonstrated minimal changes in hydrodynamic size over a three-day period (Fig. 3a). Likewise, zeta potential measurements (Fig. S8†) from day 1 to day 3 exhibited only slight variations, collectively confirming the satisfactory stability of the developed formulation. After incubating 2.6 U per mL ALP with UCNP@SiO_2-Bodipy@FFYp (50.0 μg mL^{-1}) in 0.2 M PBS (pH 7.4) at 37 °C, TEM analysis demonstrated the aggregation of nanomaterials following ALP-induced self-assembly (Fig. 3b). This observation was further validated by TEM images of the cell sections, indicating that the nanomaterials exhibited aggregation within the cellular environment (Fig. 3c). In comparison to the pre-treatment state depicted in Fig. 2c, these findings highlight the pronounced effect of ALP on the assembly behaviour of the nanomaterials.

Functionalization of UCNP@SiO_2-Bodipy with FFYp enhances cellular uptake of the nanoplatform, attributable to FFYp's targeting properties and its role in promoting cellular internalization (Fig. 3d and S9†). This modification results in heightened photo-cytotoxicity and improved cancer cell selectivity.

3.3 *In Vitro* PDT effect

The reagent 1,3-diphenylisobenzofuran (DPBF) was used as a probe to detect ROS *in vitro*. After irradiation at 980 nm with a laser, the UV-vis absorbance of DPBF at 420 nm was analyzed in different solutions. In the presence of UCNP@SiO_2-Bodipy@FFYp, a significant decrease in the UV-vis absorption of DPBF was observed within a 25-minute interval (Fig. 4a). We demonstrated the photodynamic behavior of UCNP@SiO_2-Bodipy@FFYp in HeLa cells (Fig. 4c and d) using DCFH-DA as a ROS marker. Fluorescence micrographs of DCFH-DA-stained cells showed an intense green fluorescence exclusively in cells subjected to UCNP@SiO_2-Bodipy@FFYp and laser co-treatment, indicative of an augmented generation of ROS, whereas other groups displayed no significant ROS production.

Fig. 4b demonstrates that the viability of HeLa cells (a human cervical cancer cell line) remained largely unchanged over 24, 48, and 72 hours when exposed to UCNP@SiO_2-Bodipy@FFYp at concentrations ranging from 12.50 to 200.0 μg mL^{-1}. These findings indicate that, in the absence of light irradiation, the nanomaterial exhibits negligible cytotoxicity. After laser exposure, calcein AM and PI staining micrographs

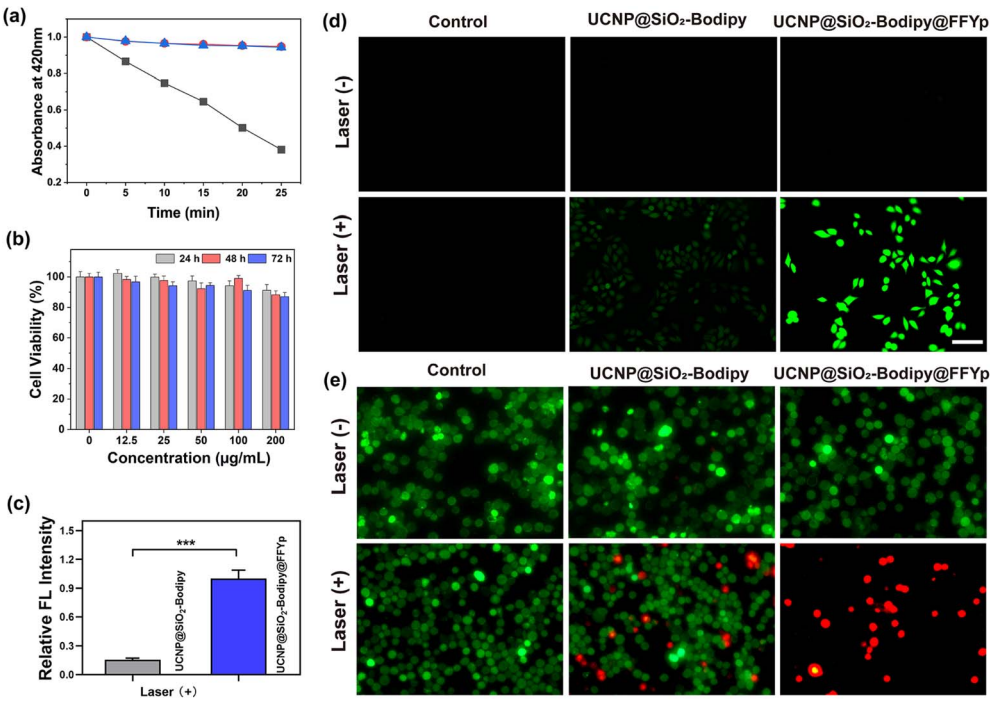

Fig. 4 PDT effect of UCNP@SiO_2-Bodipy@FFYp on cells. (a) Time-dependent bleaching curve of DPBF absorbance at 420 nm for UCNP@SiO_2-Bodipy@FFYp under 980 nm irradiation (black line), UCNP@SiO_2-Bodipy@FFYp without 980 nm irradiation (red line), and UCNP@SiO_2@FFYp under 980 nm irradiation (blue line). Data are presented as mean ± SD ($n = 3$); (b) cell viability of HeLa cells incubated with UCNP@SiO_2-Bodipy@FFYp at different concentrations for 24, 48 and 72 h. Data are presented as mean ± SD ($n = 3$); (c) corresponding ROS expression levels of UCNP@SiO_2-Bodipy@FFYp and UCNP@SiO_2-Bodipy; data are shown as mean ± SD; $n = 3$ independent experiments; (d) DCFH-DA fluorescence assay indicating the presence of intracellular ROS (scale bar: 50 μm); (e) fluorescence images of HeLa cells co-stained with calcein AM (green fluorescence) and PI (red fluorescence) after incubation with different treatments, with or without laser irradiation (scale bar: 200 μm).

(Fig. 4e) showed that UCNP@SiO_2-Bodipy@FFYp had a more pronounced inhibitory effect on HeLa cells compared to UCNP@SiO_2-Bodipy. These findings underscore the potential of UCNP@SiO_2-Bodipy@FFYp as a photosensitizer (PS) in PDT treatments.

3.4 *In vivo* PDT activity study

To evaluate the *in vivo* antitumor efficacy of UCNP@SiO_2-Bodipy@FFYp, a tumor model was established in Balb/c nude mice bearing HeLa tumors. Representative photographs of excised tumors from different treatment groups after 15 days clearly illustrated significant differences in the tumor size among groups (Fig. 5a). Mouse body weight was monitored simultaneously and exhibited no significant changes during treatment (Fig. 5b). Tumor volume was quantitatively recorded every three days throughout the treatment period, as shown in Fig. 5c. On day 15, the tumor volumes in the PBS control group and the UCNP@SiO_2-Bodipy group (with laser irradiation) markedly increased to 1012 mm^3 and 858 mm^3, respectively, suggesting no significant therapeutic effect. In contrast, the tumor volume in the UCNP@SiO_2-Bodipy@FFYp treatment group (with laser irradiation) was dramatically reduced to 39 mm^3, corresponding to a tumor inhibition rate of approximately 96.1% compared with the PBS group and 95.4% compared with the UCNP@SiO_2-Bodipy group. These findings clearly demonstrate the significant antitumor efficacy of UCNP@SiO_2-Bodipy@FFYp.

3.5 Histological analysis and biosafety *in vivo*

Histological analysis and biosafety evaluations were performed to assess both the therapeutic efficacy and systemic safety of UCNP@SiO_2-Bodipy@FFYp. Hematoxylin and eosin (HE) staining revealed that, in both the control group and the UCNP@SiO_2-Bodipy@FFYp-treated group without laser irradiation, the majority of tumor cells maintained a normal morphology with no discernible histopathological damage (Fig. 5d). Conversely, tumor cells in the UCNP@SiO_2-Bodipy@FFYp-treated group exposed to laser irradiation displayed irregular cellular structures, including karyorrhexis,

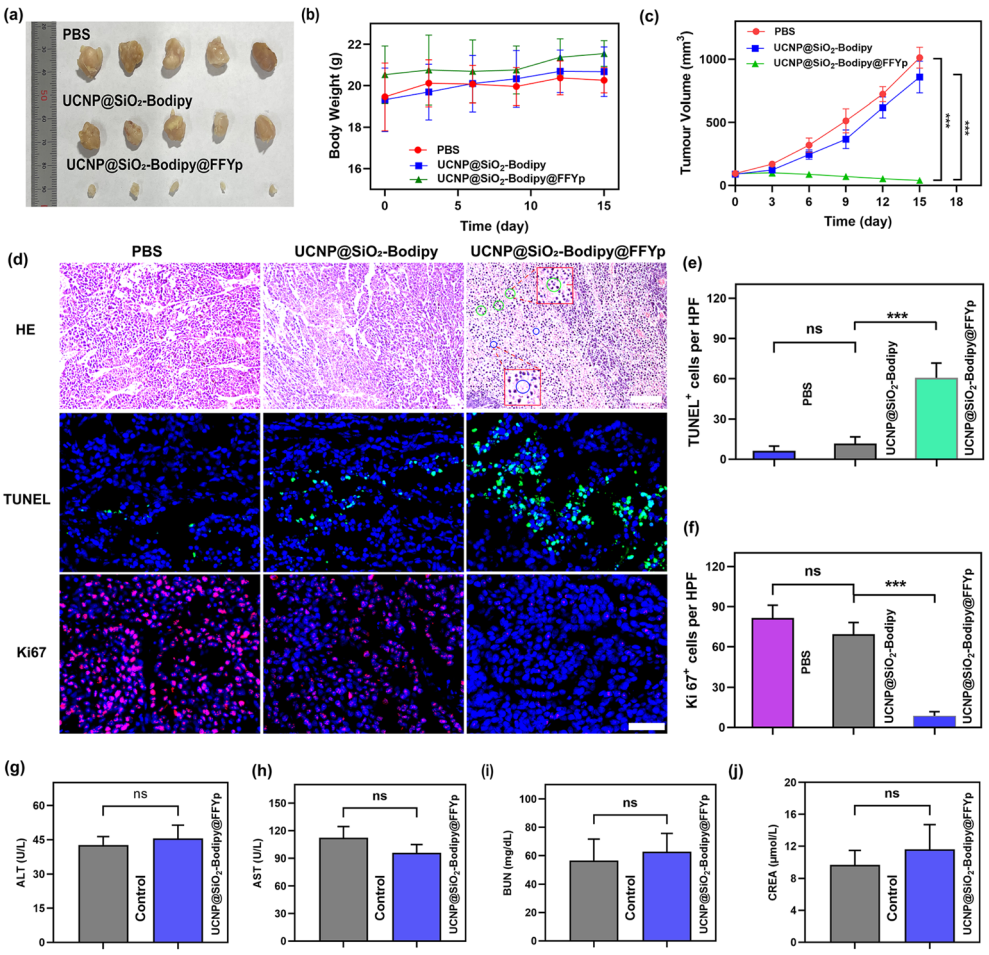

Fig. 5 PDT effect of UCNP@SiO_2-Bodipy@FFYp on tumors. (a) Photographs of excised tumors (day 15); (b) tumor volume; (c) mouse body weight; (d) HE staining (green circles indicate pyknosis, blue circles indicate karyorrhexis, and scale bar: 50 μm), TUNEL and Ki67 staining (scale bar: 20 μm); (e) mean number of TUNEL positive cells per high-power field (HPF) in the tumor was analyzed among groups; (f) mean number of Ki67 positive cells per HPF in the tumor was analyzed among groups; (g–j) liver function assays (alanine aminotransferase (ALT, (g)), aspartate aminotransferase (AST, (h)), blood urea nitrogen (BUN, (i))) and kidney function assays (creatinine (CREA, (j)) after injection of UCNP@SiO_2-Bodipy@FFYp for 3 days. *P* values were determined by the two-tailed Student's *t*-test, ns, $P > 0.05$; ***$P < 0.001$.

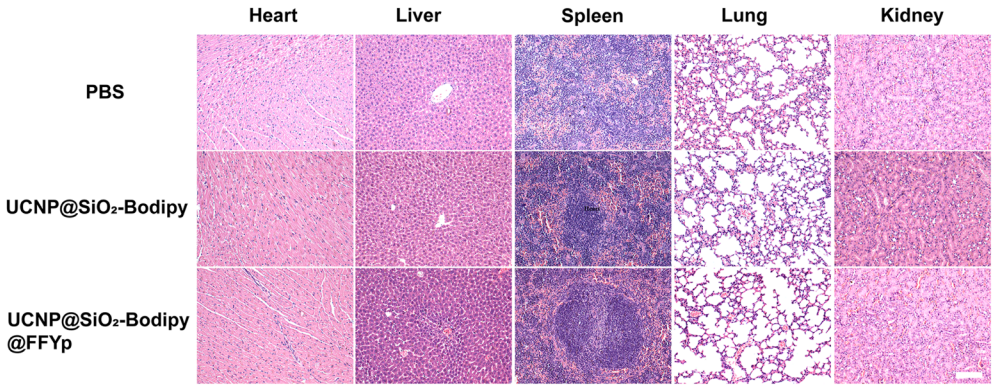

Fig. 6 HE staining of the heart, liver, spleen, lungs, and kidneys isolated from mice after various treatments. Scale bar: 50 μm.

pyknosis, and karyolysis, indicating substantial tumor cell ablation. These observations were corroborated by terminal deoxynucleotidyl transferase dUTP nick-end labeling (TUNEL) and Ki67 staining (Fig. 5d–f), which demonstrated pronounced tumor cell apoptosis and a marked reduction in proliferative activity. Additionally, toxicity assessments—encompassing body weight monitoring (Fig. 5b), liver and kidney function evaluations (Fig. 5g–j), routine blood tests (Fig. S10†), and HE staining of major organs (Fig. 6)—showed minimal signs of tissue damage or inflammation, reflecting the excellent biocompatibility of UCNP@SiO_2-Bodipy@FFYp *in vivo*.

ICP-MS analysis was conducted to measure Y concentrations in different organs of BALB/c nude mice bearing HeLa tumors after injection of UCNP@SiO_2-Bodipy@FFYp and UCNP@SiO_2-Bodipy (Fig. S11†). The results revealed that, apart from tumor tissues, UCNP@SiO_2-Bodipy@FFYp was also enriched in the liver and kidneys, likely due to their key metabolic functions. However, ALP expression in these normal tissues was notably lower than in HeLa tumors (Fig. S12, ESI†). Moreover, significantly higher Y accumulation in tumors treated with UCNP@SiO_2-Bodipy@FFYp compared to UCNP@SiO_2-Bodipy further indicates improved tumor-selective activation. These data collectively suggest that the developed formulation achieves selective activation in tumor cells with minimal potential for off-target effects.

4. Conclusions

In summary, we developed a UCNP@SiO_2-Bodipy@FFYp core–shell–shell nanoplatform that not only aggregates selectively within tumor cells but also enables NIR-induced PDT with deep-tissue penetration. This was accomplished by coating upconversion nanoparticles with a silica shell embedded with Bodipy-I photosensitizers, followed by covalent conjugation of the targeting peptide FFYp. The Bodipy-I photosensitizers, which exhibit robust ROS-generating capacity, undergo FRET driven by the UCNP emission. Furthermore, NIR illumination overcomes the inherent limitation of Bodipy-I's dependence on visible-light excitation, thus achieving deeper tumor penetration. Once introduced into the tumor microenvironment, the FFYp peptide on the nanoparticle surface is dephosphorylated by highly expressed alkaline phosphatase, promoting selective tumor accumulation.

In comparison with conventional photosensitizers[35] or other nanoparticle-based PDT systems,[36] UCNP@SiO_2-Bodipy@FFYp offers two distinct advantages: (i) in contrast to visible-light-based photosensitizers, the use of NIR light enables deeper tissue penetration and significantly enhances therapeutic efficacy and safety in tumor treatment, and (ii) ALP-triggered tumor specificity effectively reduces off-target effects, thereby improving the overall therapeutic outcome.

Data availability

The original contributions presented in the study are included in the article; further inquiries can be directed to the corresponding author.

Author contributions

Bo Ling: methodology, investigation, formal analysis, writing – original draft. Yaguang Wang: methodology, formal analysis. Huaze Dong: methodology. Hongqi Chen: writing – review & editing, funding acquisition. Lun Wang: supervision, funding acquisition. All authors read and approved the final manuscript.

Conflicts of interest

There are no conflicts to declare.

Acknowledgements

This work was supported by the National Natural Science Foundation of China (21675002), the Natural Science Foundation of the Higher Education Institutions of Anhui Province (2022AH052123, 2022AH052165 and 2023AH050139), and the Transverse Research Fund of Hefei Normal University (50122021).

References

1 J. Li, Y. Tian and T. Zheng, *Chem. Commun.*, 2022, **58**, 6542–6545.
2 T. C. Pham, V. N. Nguyen, Y. Choi, S. Lee and J. Yoon, *Chem. Rev.*, 2021, **121**, 13454–13619.
3 X. Wang, M. Wu, X. Zhang, F. Li, Y. Zeng, X. Lin, X. Liu and J. Liu, *J. Nanobiotechnol.*, 2021, **19**, 204.
4 N. Singh, R. Sen Gupta and S. Bose, *Nanoscale*, 2024, **16**, 3243–3268.
5 X. Deng, Z. Shao and Y. Zhao, *Adv. Sci.*, 2021, **8**, 2002504.
6 D. Wei, Y. Chen, Y. Huang, P. Li, Y. Zhao, X. Zhang, J. Wan, X. Yin, T. Liu, J. Yin, Z. Liu, Q. Zhang, J. Wang and H. Xiao, *Nano Today*, 2021, **41**, 101288.
7 T. Liu, C. Wang, W. Cui, H. Gong, C. Liang, X. Shi, Z. Li, B. Sun and Z. Liu, *Nanoscale*, 2014, **6**, 11219–11225.
8 Y. Cen, W. Deng, Y. Yang, R. Yu and X. Chu, *Anal. Chem.*, 2017, **89**, 10321–10328.
9 D. Wang, M. Lee, G. Shan, R. Kwok, J. Lam, H. Su, Y. Cai and B. Tang, *Adv. Mater.*, 2018, **30**, 1802105.
10 N. M. Idris, M. K. Gnanasammandhan, J. Zhang, P. C. Ho, R. Mahendran and Y. Zhang, *Nat. Med.*, 2012, **18**, 1580–1585.
11 T. Yu, D. Wei, Z. Li, L. Pan, Z. Zhang, Z. Tian and Z. Liu, *Chem. Commun.*, 2020, **56**, 1976–1979.
12 G. Lu, X. Gao, H. Zhang, Y. Zhang, Y. Yu, Z. Sun, W. Li, W. Wu, Y. Lu and H. Zou, *Chin. Chem. Lett.*, 2022, **33**, 1923–1926.
13 J. He, C. Li, L. Ding, Y. Huang, X. Yin, J. Zhang, J. Zhang, C. Yao, M. Liang, R. P. Pirraco, J. Chen, Q. Lu, R. Baldridge, Y. Zhang, M. Wu, R. L. Reis and Y. Wang, *Adv. Mater.*, 2019, **31**, 1902409.
14 Y. Xu, J. Yu, J. Hu, K. Sun, W. Lu, F. Zeng, J. chen, M. liu, Z. Cai, X. He, W. Wei and B. Sun, *Adv. Healthcare Mater.*, 2023, **12**, 2203080.
15 N. Yu, L. Huang, Y. Zhou, T. Xue, Z. Chen and G. Han, *Adv. Healthcare Mater.*, 2019, **8**, 1801132.
16 A. Hak, M. S. Ali, S. A. Sankaranarayanan, V. R. Shinde and A. K. Rengan, *ACS Appl. Bio Mater.*, 2023, **6**, 349–364.
17 N. Hodgkinson, C. A. Kruger, M. Mokwena and H. Abrahamse, *J. Photochem. Photobiol., B*, 2017, **177**, 32–38.
18 P. Wang, B. Wang, L. Zhang, X. Liu, L. Shi, X. Kang, X. Lei, K. Chen, Z. Chen, C. Li, C. Zhang, P. Tu, M. Pan, Q. Ju, X. Man, Y. Lu, N. Yu, Y. Li, H. Zhu, R. Zhang, J. Su, S. Tao, J. Qiao, Q. Mu, W. Zeng, Z. Li, Y. Gao, H. Gu and X. Wang, *Photodiagn. Photodyn.*, 2023, **41**, 103261.
19 W. Sun, L. Luo, Y. Feng, Y. Qiu, C. Shi, S. Meng, X. Chen and H. Chen, *Adv. Mater.*, 2020, **32**, 2000377.
20 S. Mohanty and A. M. Kaczmarek, *Chem. Soc. Rev.*, 2022, **51**, 6893–6908.
21 J. Zhou, Q. Liu, W. Feng, Y. Sun and F. Li, *Chem. Rev.*, 2015, **115**, 395–465.
22 L. Wang, R. Yan, Z. Hao, L. Wang, J. Zeng, J. Bao, X. Wang, Q. Peng and Y. Li, *Angew. Chem., Int. Ed.*, 2005, **44**, 6054–6057.
23 E. Hemmer, M. Quintanilla, F. Légaré and F. Vetrone, *Chem. Mater.*, 2015, **27**, 235–244.
24 Y. Li, X. Liu, X. Zhang, W. Pan, N. Li and B. Tang, *Chem. Commun.*, 2021, **57**, 12087–12097.
25 K. Tezuka, M. Umezawa, T. I. Liu, K. Nomura, K. Okubo, H.-C. Chiu, M. Kamimura and K. Soga, *ACS Appl. Bio Mater.*, 2021, **4**, 4462–4469.
26 J. Xu, L. Xu, C. Wang, R. Yang, Q. Zhuang, X. Han, Z. Dong, W. Zhu, R. Peng and Z. Liu, *ACS Nano*, 2017, **11**, 4463–4474.
27 R. Lv, M. Raab, Y. Wang, J. Tian, J. Lin and P. N. Prasad, *Coord. Chem. Rev.*, 2022, **460**, 214486.
28 G. Bassi, N. Favalli, C. Pellegrino, Y. Onda, J. Scheuermann, S. Cazzamalli, M. G. Manz and D. Neri, *J. Med. Chem.*, 2021, **64**, 15799–15809.
29 Y. Hu, Y. Miao, J. Zhang, Y. Chen, L. Qiu, J. Lin and D. Ye, *Nano Lett.*, 2021, **21**, 10377–10385.
30 F. Ma, M. Liu and C. Zhang, *Chem. Commun.*, 2019, **55**, 8963–8966.
31 L. Dong, Q. Miao, Z. Hai, Y. Yuan and G. Liang, *Anal. Chem.*, 2015, **87**, 6475–6478.
32 W. Xia, B. Ling, L. Wang, F. Gao and H. Chen, *Chem. Commun.*, 2020, **56**, 8440–8443.
33 L. Huang, J. Zhao, S. Guo, C. Zhang and J. Ma, *J. Org. Chem.*, 2013, **78**, 5627–5637.
34 D. Zhu, Z. Y. Miao, Y. Hu and X. J. Zhang, *Biosens. Bioelectron.*, 2018, **100**, 475–481.
35 M. Luo, H. Li, D. Han, K. Yang and L. Kang, *Photodiagn. Photodyn.*, 2021, **36**, 102605.
36 J. Xu, W. Zhang, Y. Guo, X. Chen and Y. Zhang, *Drug Delivery*, 2022, **29**, 664–678.